Nanoscale

PAPER

View Article Online
View Journal | View Issue

Cite this: *Nanoscale*, 2021, **13**, 2429

Superradiative plasmonic nanoantenna biosensors enable sensitive immunoassay using the naked eye†

Yang Xiong,[a] Tong Fu,[b] Daxiao Zhang,[b] Shunping Zhang *[b] and Hongxing Xu*[a,b]

Received 25th August 2020,
Accepted 26th December 2020

DOI: 10.1039/d0nr06148d

rsc.li/nanoscale

Easy-to-use and sensitive quantification of biomarkers has a great significance in disease prediction, diagnosis, and monitoring. Here, we report a biosensor for simple and sensitive biomarker detection based on the strong light scattering (brightness) of superradiative plasmonic nanoantennas. This nanoantenna is constructed using antibody-decorated gold nanoparticles (Au NPs) immobilized onto a gold mirror by the target antigen, forming a nanoparticle-on-mirror (NPOM) configuration. The NPOM produces an order of magnitude stronger light scattering in the red region compared with isolated Au NPs on the dielectric substrate, due to the strong near-field coupling of surface plasmons across the gap between the Au NPs and the gold film. The increased brightness allows one to observe the captured Au NPs with the naked eye using a dark-field optical microscope. The particle density of the Au NPs varies linearly with the concentration of the target antigen over a broad dynamic range from 10^{-3} to 10^{3} ng mL^{-1}. This dynamic range is three orders of magnitude broader than that obtained from the previous work based on a dark-field optical microscope. The limit of detection is 1 pg mL^{-1} (6.67 fM), which is three orders of magnitude more sensitive than that obtained in the previous work using similar conditions. The uniform spatial distribution of the Au NPs on the gold film was allowed to quantify biomarkers with a relative standard deviation as small as 1–7%. Biosensing using superradiative NPs can lower the detection limit, simplify, and speed up the detection procedure for biomarker detection.

Introduction

Simple, sensitive, and cost-effective detection of biomarkers is most desirable for biosensing. Among various detection methods, immunoassay is one of the most sensitive analytical tools based on the specific recognition between antibodies and antigens. In recent years, immunoassay has become a powerful analytical tool in many applications, such as food safety,[1] disease diagnosis,[2] and environmental monitoring.[3] Efficient signal readout of immunoassays has been well developed using different strategies, including the enzyme-linked immunosorbent assay,[2,4] surface-enhanced Raman scattering (SERS),[5–7] fluorescence,[8–10] surface plasmon resonance,[11–14] and electrochemistry.[15] Although the above-mentioned methods are well developed for biomarker detection, there are still several limitations, *e.g.*, poor sensitivity, high cost of instrumentation, and a time-consuming labelling and signal collection process. Therefore, it is highly desirable to find a simple, low-cost, and sensitive strategy for biomarker detection.

Noble metal nanoparticles (NPs) have attracted a lot of attention due to their plasmonic properties.[16] Under the excitation of visible or near-infrared light, metal NPs exhibit strong light absorption or scattering at certain wavelengths due to localized surface plasmon resonances. As a result, NPs show different colours under an optical dark-field microscope (DFM).[17,18] Together with a recording camera on the microscope, DFM can be used as a simple, sensitive, and low-cost technique to detect the concentration of NPs, down to a single NP level. By functionalizing NPs with specific capture agents, DFM can be used to quantify the concentration of biomarkers based on counting the number of NPs.[19–22] By real-time monitoring the dark-field scattering spectra of NPs, DFM can also be used to probe the change of refractive index around the NPs[23] or even the adsorption process of a single target analyte.[24,25] However, counting the number of NPs in DFM may not be an easy task because background scattering noise from the sample matrix or dust on the substrate surface can significantly reduce the signal-to-noise ratio. The key to this problem is that the scattering intensity of a single metal NP on a typical glass or silicon substrate is not strong enough due to

[a]*The Institute for Advanced Studies, Wuhan University, Wuhan 430072, China. E-mail: hxxu@whu.edu.cn*
[b]*School of Physics and Technology, Center for Nanoscience and Nanotechnology, and Key Laboratory of Artificial Micro- and Nano-structures of Ministry of Education, Wuhan University, Wuhan 430072, China. E-mail: spzhang@whu.edu.cn*

†Electronic supplementary information (ESI) available. See DOI: 10.1039/d0nr06148d

the limited dipole moment of the surface plasmon resonances. As a result, the sensitivity and reproducibility of DFM-based biosensing *via* NP counting are generally limited.

Here, we use a nanoparticle-on-mirror (NPOM)[16,26–30] system to overcome these drawbacks to quantify the concentration of human immunoglobulin G (IgG) by counting the number of Au NPs immobilized on the gold film in the DFM image. The concentrations of IgG are quantified over a broad dynamic range from 10^{-3} to 10^{3} ng mL^{-1}, using the NPOM system consisting of antibody-conjugated Au NPs, an antigen, and an antibody-conjugated gold film. The strong light scattering of the NPOM system makes the Au NPs very bright in the DFM image so that they can be easily observed with the naked eye. The background is thus suppressed and it is easier to count the number (particle density) of Au NPs in a given region. The sensitivity of this plasmonic nanoantenna biosensor is down to 1 pg mL^{-1} (6.67 fM), which is three orders of magnitude more sensitive than that obtained in the previous work using a DFM-based immunoassay.[19,31]

Results and discussion

The composite structure of Au NPs on a gold film (Fig. 1a) can be regarded as a plasmonic nanogap antenna.[26] The coupling between the Au NPs and gold film results in the enhancement of near fields and increases the scattering efficiency of radiative modes.[32] Fig. 1b compares the experimental dark-field scattering spectra of a Au NP on top of a gold film or silicon substrate (covered with a 285 nm SiO_2 layer). The strong localized surface plasmon resonance peak of the NPOM system is at 676 nm, which is usually called bright nanoantenna mode since it is originated from the bonding coupling between the electric dipole of the NP and its image in the gold film.[33] For comparison, the resonance peak of a similar size Au NP on the SiO_2 substrate is at 533 nm, and the scattering is much weaker over the entire spectrum. In the spectral window of 650–700 nm used in this work, the scattering of the Au NP on the SiO_2 substrate is as weak as the noise level, while the NPOM system reaches the most intense brightness.

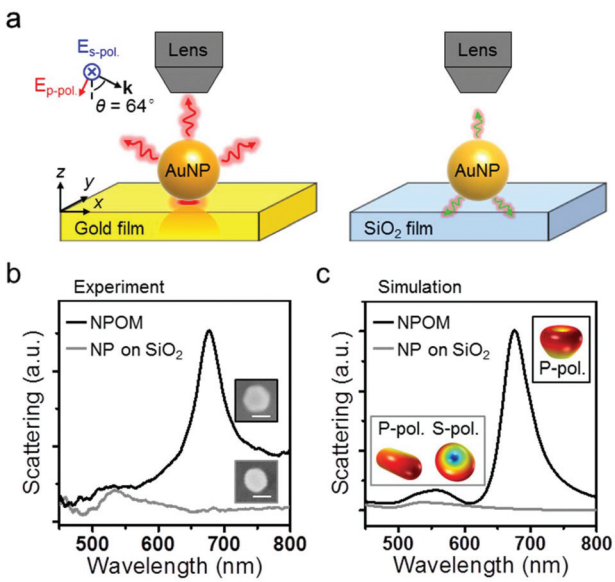

Fig. 1 (a) Schematic of light scattering by Au NPs on a gold film and a SiO_2 substrate. (b) Measured dark-field scattering spectra of Au NPs on a gold film and a SiO_2 substrate. The inset shows the scanning electron microscopy images of the two Au NPs. Scale bars are 50 nm. The diameters of the Au NPs are 65 nm (on gold film) and 60 nm (on SiO_2). (c) Simulated unpolarized scattering spectra of Au NPs on a gold film and a SiO_2 substrate. The insets show the far-field scattering pattern of Au NPs on a gold film (black frame, peak at 676 nm) and a SiO_2 substrate (gray frame, peak at 530 nm (p-pol.) and 570 nm (s-pol.)).

A quantitative comparison of the scattering for a Au NP on the two substrates can be accomplished by electromagnetic modelling. The simulated dark-field scattering spectra (Fig. 1c) of a Au NP on a gold film and SiO_2 substrate match quite well with the experimental results. According to the experimental configuration, an oblique incidence of unpolarized light contains both p- and s-polarized waves that can excite both the horizontal and vertical electric dipoles. The simulated dark-field spectra were modelled by adding up the spectra under p- and s-polarized light excitation. The scattering intensity is much stronger when the Au NP is placed on the gold film due to the strong near-field interaction between them. On the one hand, the end-to-end bonding of the electric dipole in the Au NP and its electromagnetic image in the metallic mirror produce a big dipole that couples strongly to free space light. Compared with an isolated Au NP, there are more conduction electrons involved in the collective oscillations in the NPOM since those from the gold film can also take part in. This contributes to a larger oscillator strength of the system. On the other hand, the far-field scattering of the bright dipole mode is mainly to the upward around 60° to the substrate normal (the inset in Fig. 1c, black frame) because of the appearance of the gold film.[16] Such an upward doughnut shape of the far-field scattering pattern increases the collection efficiency of the scattered light by a typical high NA microscope objective.[32] In contrast, light is mainly scattered into the substrate side for Au NPs on the SiO_2 substrate for both p- and s-polarized light excitation, as shown in the far-field scattering pattern (the inset in Fig. 1c, gray frame). Note that only the p-polarized light can excite the bonding dipole mode for the NPOM. The scattering intensity under unpolarized light excitation is dominant by the p-polarized component so that scattering under s-polarized light excitation can be negligible (ESI Fig. S1†). Under unpolarized light excitation, the scattering intensity of the peak in the NPOM is almost 20.5 times greater than the peak intensity of a Au NP on SiO_2. Therefore, this NPOM system makes the Au NPs very bright and easier to observe with the naked eye in DFM.

Fig. 2 shows the surface modification process of the Au NPs and the gold film, and a sandwich structure is formed in the end by linking the three components of antibody-conjugated Au NPs, an antigen, and an antibody-conjugated gold film. Au NPs and gold films are often used for bioassay because of

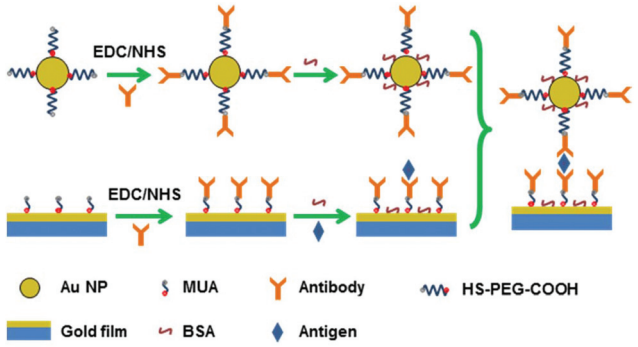

Fig. 2 Schematic illustration of the process of forming a sandwich structure through an immunoassay protocol. MUA: 11-mercaptoundecanoic acid; EDC: 1-ethyl-3-(3-dimethyllaminopropyl) carbodiimide hydrochloride; NHS: *N*-hydroxysuccinimide; BSA: bovine serum albumin.

their better stability and biocompatibility. In the first step, Au NPs are modified with HS-PEG-COOH and mPEG-SH molecules, and gold films are modified with 11-mercaptoundecanoic acid (MUA) molecules. These molecules can easily bind to the Au NPs and the gold film by sulfhydryl groups. The mPEG-SH molecules on the surface of Au NPs can not only prevent the aggregation of Au NPs especially in the presence of salt buffer solution, but also eliminate nonspecific adsorption.[34,35] In the second step, the antibodies are linked to the Au NPs and the gold film. First, the carboxyl groups of HS-PEG-COOH modified on Au NPs and MUA modified on the gold film are activated by 1-ethyl-3-(3-dimethyllaminopropyl) carbodiimide hydrochloride (EDC) and *N*-hydroxysuccinimide (NHS). Then the antibody solution is added to the Au NP solution and dropped onto the surface of the gold film. The antibodies will bind to the Au NPs and the gold film by a dehydration condensation reaction. The third step is blocking and antigen capture. Bovine serum albumin (BSA) is used to block these unreacted sites on the Au NPs and gold film to avoid nonspecific absorption. Then the target antigen is added to the antibody-conjugated gold films and identified by the antibody–antigen specific reaction. The last step is to form a sandwich structure. The antibody-conjugated Au NP solution is added onto the prepared gold film, and Au NPs will be bound to the gold film by reacting with these captured antigens. Therefore, with the increasing concentration of target antigen, there will be more Au NPs immobilized on the gold film. Using the number of Au NPs in the dark-field image as a function of antigen concentration, trace amounts of antigen can be detected.

Fig. 3a shows the experimental setup for DFM. White light is illuminated onto the sample, and the Rayleigh scattering

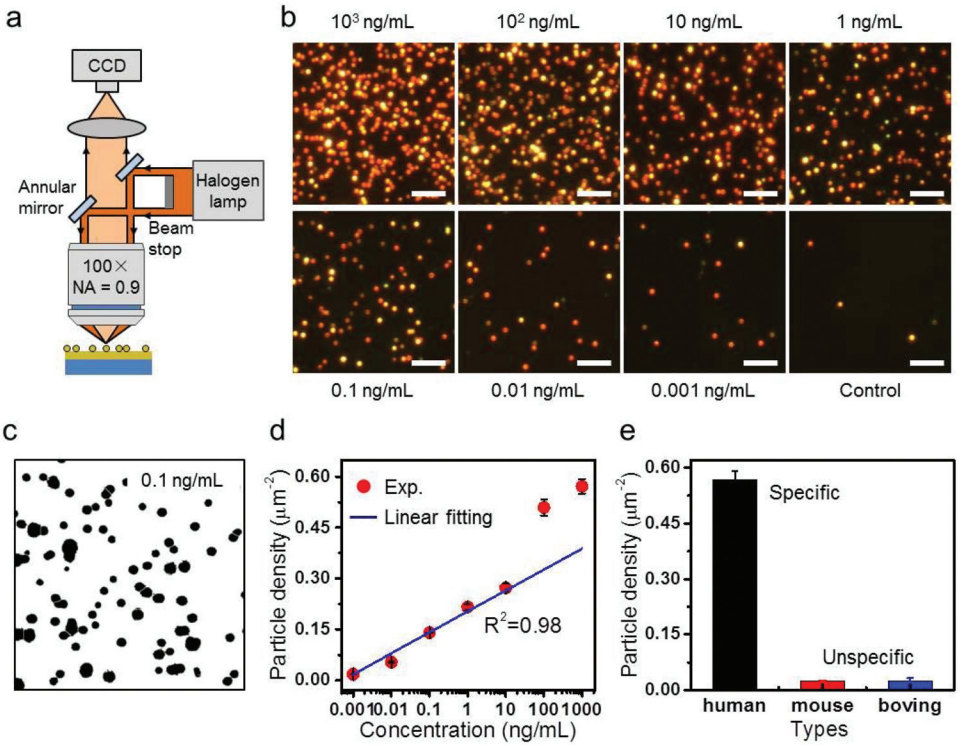

Fig. 3 (a) Experimental setup for dark-field microscopy (DFM). (b) Dark-field images of Au NPs bound to the gold film with different concentrations of human IgG. The dynamic range is from 10^{-3} to 10^{3} ng mL^{-1}. The control sample uses 0 ng mL^{-1} of human IgG. Scale bars are 5 μm. (c) The grayscale image of the DFM image with 0.1 ng mL^{-1} human IgG. (d) The plot of the particle density of Au NPs on the gold film as a function of the concentration of human IgG. Error bars indicate the standard deviations from 5 measurements. (e) The specificity of this DFM biosensor. The concentrations of human IgG, mouse IgG, and bovine IgG are all 10^{3} ng mL^{-1}. Error bars indicate the standard deviations from five measurements.

light from the Au NPs is then directed onto the CCD camera and several bright spots can be found with the naked eye in DFM. It only takes a few milliseconds to record a dark-field image, which is faster than the acquirement of Raman or fluorescence spectra, especially a mapping image. Fig. 3b shows the dark-field images of Au NPs immobilized on the gold film at different concentrations of human IgG through an immunoassay protocol (the whole DFM images are shown in ESI Fig. S2†). The scattering light from the NPOM is red, which is consistent with the scattering spectra (Fig. 1b). The distribution of Au NPs is uniform and the aggregates are barely formed. It is obvious that with the increase of antigen concentration, there are more bright spots in the dark field image, which means that more Au NPs were bound to the gold film. The number of Au NPs immobilized on the gold film saturates when the concentration of human IgG is 1 μg mL^{-1}, reaching a density of 0.57 μm^{-2}, corresponding to an average distance of 1.3 μm between adjacent Au NPs.

The number of particles in the dark-field images is counted using ImageJ software (National Institutes of Health). The image is first converted into a grayscale image, and then the particles are counted. Fig. 3c shows the grayscale image of the DFM image with 0.1 ng mL^{-1} human IgG. Using the "watershed" function of ImageJ, adjacent particles can be distinguished, which could increase the accuracy of counting the number of particles. Fig. 3d shows the particle density of Au NPs as a function of the concentration of human IgG with a broad dynamic range from 10^{-3} to 10^{3} ng mL^{-1} (6.67 nM–6.67 fM). The calibration curve shows a good linear response in this broad dynamic range, where the linear correlation coefficient (R^2) is 0.98. It should be noted that the correlation coefficient is 0.99 when a linear fitting is performed at concentrations from 10^{-3} to 10 ng mL^{-1}. The limit of detection of the biosensor is defined when the signal at this concentration is three times larger than the standard deviation of a control sample (without the target antigen). Therefore, the limit of detection of this biosensor is down to 1 pg mL^{-1} (6.67 fM). Compared with the previous studies based on DFM, the limit of detection in this work is comparable to the best reported one, while the dynamic range is broader by three orders of magnitude (Table 1). The comparison of the lowest limit of detection of IgG using different detection methods based on the immunoassay is listed in Table S1 (ESI†). This work is more sensitive than the previous works based on surface plasmon resonance and dark-field microscopy. Although SERS and electrochemistry are more sensitive, the DFM-based method is simpler and cost-effective.

Relative standard deviation can reflect the spatial distribution of NPs. As shown in Fig. 3d and Table S2 (ESI†), the relative standard deviations of five measurements over an area of 774 μm^2 for different concentrations are very small, which indicates that the distribution of Au NPs on gold films is uniform. The specificity of a biosensor is also very important in biomarker detection. Unspecific antigen mouse IgG and bovine IgG at a high concentration of 10^3 ng mL^{-1} are used to test the specific interaction for this biosensor. As shown in Fig. 3e, the particle densities for 10^3 ng mL^{-1} mouse IgG and bovine IgG are both 0.025 μm^{-2}, which are almost similar to that using a 6 order-lower-concentration of human IgG. This indicates that the nonspecific absorption is low. Therefore, this biosensor has the ability of specific recognition for biomarker detection. The residual particle density (in an ideal case, it is zero) does not tend to zero because even if the concentration of a specific antigen is zero, some Au NPs will still be adsorbed on the surface of the gold film by gravity or electrostatic adsorption. Besides, dust particles on the surface of the gold film will also make the residual particle density larger. Integrating the sample with a microfluidic chip or improving the collection optics like adding a band-pass filter on the optical path can in principle lower this background density.

The size of the Au NPs is an important affecting factor in this DFM-based immunoassay. Selecting Au NPs with an appropriate size is not only conducive to observation but also can improve the signal-to-noise ratio. The scattering intensity of Au NPs is proportional to the sixth power of its size. So a larger Au NP has a stronger scattering intensity and in principle, it can be easily observed in DFM. However, with the increase of the particle size, the resonance wavelength gets redshifted to the near infrared region. Noting that the response curve of a typical commercial CCD camera is maximized in the visible region (~550 nm), Au NPs with a strong scattering and resonance wavelength in the visible region (<700 nm) will be the best candidate.

Fig. 4 shows the dark-field scattering spectra and dark-field images of the NPOM with 40, 60, 80, and 100 nm Au NPs. 1 nm Al_2O_3 was used as the spacer layer between the Au NP and gold film. It is obvious that with the increase of the particle size, the scattering becomes stronger and the resonance wavelength gets redshifted and approaches the infrared region. The resonance wavelength of 40 nm Au NPs on the gold film approaches 600 nm (Fig. 4a), while the scattering is weak in the dark-field image (Fig. 4b). The scattering of 100 nm Au NPs is very strong, but the resonance wavelength is more than 800 nm, resulting in low brightness of the Au NPs in the dark-field image. The scattering of 60 and 80 nm Au NPs is strong, and their resonance wavelengths are between 650 and 700 nm. They are bright and can be easily observed in the dark-field images (Fig. 4b). In reality, the 60 nm Au NP is slightly prior to the 80 nm one. This is because the resonance wavelength of

Table 1 Comparison of biomarker detection based on DFM

Biomarker	Limit of detection	Dynamic range	Ref.
AFP	7.25 pM	7.25 pM–1.25 nM	19
Pyrophosphate	1.49 nM	0–4.29 μM	20
Permanganate	46 nM	0–6 μM	21
DNA	3 fM	20 pM–20 nM	22
CEA	1.7 pM	0–300 pM	31
IgG	6.67 fM	6.67 fM–6.67 nM	This work

AFP: alpha fetoprotein; CEA: carcinoembryonic antigen.

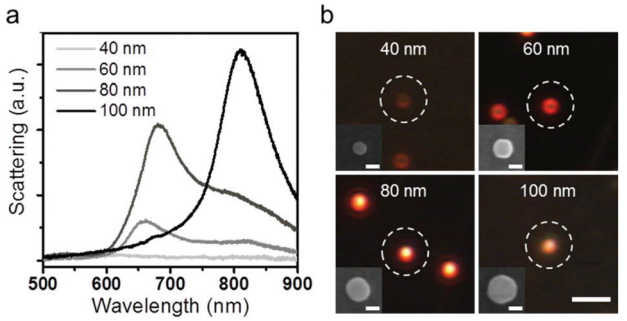

Fig. 4 Dark-field scattering spectra (a) and dark-field images (b) of the NPOM with 40, 60, 80, and 100 nm Au NPs. 1 nm Al_2O_3 was used as the spacer layer. The scale bar, applied to all four images, is 2 μm. The inset shows the scanning electron microscopy images of the Au NPs, and the scale bars are 50 nm.

the 80 nm sample is closer to the detection limit of the CCD. A small fluctuation in the size of Au NPs or the gap between the Au NP and gold film, *etc*. will shift the plasmon resonance outside the detection range of the camera. What's more, the doughnut shape of the 60 nm Au NP in the dark-field image (Fig. 4b) makes it easy to be distinguished from others like dust particles, which could further improve the signal-to-noise ratio.

SERS-based immunoassay is another powerful tool for biomarker detection[36] with high sensitivity.[37–39] It uses the Raman intensity of the Raman molecules as the readout signal, unlike the DFM-based immunoassay which used the elastic light scattering as readout. To better show the priority of the DFM-based immunoassay, we compare the sensitivity and relative standard deviation of these two methods based on an equal footing, since the NPOM configuration can also provide an excellent enhancement for Raman molecules inside the gap region between the Au NP and the gold film.[16,26,29,40]

Fig. 5a shows the SERS spectra recorded for different concentrations of human IgG. The detection range is from 0.1 to 10^3 ng mL^{-1}. The Raman bands at 1076 and 1587 cm^{-1} are the characteristic peaks of 4-mercaptobenzoic acid (4-MBA) molecules. Based on the definition of the limit of detection, the limit of detection of the SERS-based immunoassay is only 0.1 ng mL^{-1}, which is two orders of magnitude lower than that of the DFM-based immunoassay. The reason for the lower sensitivity is that the modification of Raman molecules on the surface of Au NPs will reduce the number of active sites for antibody conjugation.[41] Besides, the monodispersity of Au NPs becomes worse when the Raman molecules were added to the Au NP solution, resulting in a decrease in the number of Au NPs bound to the gold film (shown in ESI Fig. S3†). Direct comparison of the two methods is shown in Fig. 5b since both data were taken from the same sample. It is clear that the linearity of the signal is higher when using the particle density as readout than using the Raman intensity. In terms of reproducibility, the relative standard deviations (obtained from repeated measurements) of the peak intensity at 1587 cm^{-1} are also larger than that from the DFM-based immunoassay (Fig. 5b and Table S2 in the ESI†).

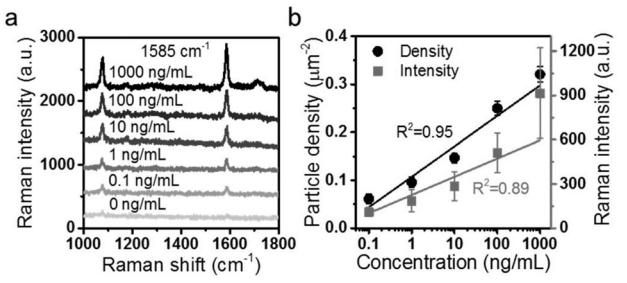

Fig. 5 (a) SERS spectra of the SERS-based immunoassay with different concentrations of human IgG. (b) The plot of the particle density and SERS intensity at 1587 cm^{-1} as a function of the concentration of human IgG. Error bars indicate the standard deviations from five measurements.

Conclusions

A simple, low-cost, and sensitive biosensor based on a NPOM system to quantify the concentration of biomarkers has been proposed, by simply replacing the dielectric substrate in traditional DFM by a gold film. The coupling between the Au NPs and gold film results in an increase in the scattering efficiency of radiative modes and makes the Au NPs very bright in DFM. The concentrations of the biomarker can be quantified by the number of Au NPs immobilized on the gold film. A low limit of detection of 1 pg mL^{-1} (6.67 fM) and a broad dynamic range from 10^{-3} to 10^3 ng mL^{-1} were obtained, which is superior to those obtained in the previous work based on DFM. The specificity of the biosensor was also demonstrated. Compared with the SERS-based immunoassay, the DFM-based immunoassay is more sensitive and has a broader dynamic range and better reproducibility. This biosensor could also be used for the detection of other biomarkers, and the use of different metal NPs (different sizes, materials, and shapes) enables it to have multiplexed biomarker detection capabilities. It has the ability to detect IgG and IgM antibodies simultaneously, *e.g.* for corona virus.

Experimental methods

Materials

11-Mercaptoundecanoic acid (MUA) and 4-mercaptobenzoic acid (4-MBA) were purchased from Sigma-Aldrich. Thiol PEG acid (HS-PEG-COOH, MW 3400), thiol PEG (mPEG-SH, MW 5000), 1-ethyl-3-(3-dimethylaminopropyl)carbodiimide hydrochloride (EDC), and *N*-hydroxysuccinimide (NHS) were purchased from Aladdin Chemistry Co., Ltd (Shanghai, China). Bovine serum albumin (BSA) and phosphate-buffered saline (PBS, 1×, PH 7.4) buffer solution were purchased from Beyotime. Human IgG (Catalog bs-0297P), mouse IgG (Catalog bs-0296P), bovine IgG (Catalog bs-0326P), and goat anti-human IgG antibody (Catalog bs-0297G) were purchased from

Beijing Biosynthesis Biotechnology Co., Ltd. Au NP solution (40, 60, 80, and 100 nm diameter) was purchased from BBI solutions. Deionized water (18.3 MΩ cm^{-1}) was used in the experiments. All other reagents were of analytical reagent grade and were used without further purification.

Sample preparation

For the preparation of a gold film, a 10 nm-thick chromium film was first evaporated on clean silicon wafers (0.7 × 0.7 cm) through thermal evaporation deposition. The deposition rate was kept at 0.5 Å s^{-1}. Then a 100 nm-thick gold film was evaporated, and the deposition rate was kept at 0.5 Å s^{-1}.

The process of preparation of antibody conjugated Au NPs is shown in Fig. 2. First, 30 μL of 10 μM HS-PEG-COOH linker was added to 500 μL of Au NP solution at room temperature. After shaking for 30 min, 60 μL of 10 μM mPEG-SH solution was added and stored at 4 °C for 12 h. Then the mixture was centrifuged at 6000 rpm for 6 min to remove the excess HS-PEG-COOH and mPEG-SH, and then resuspended in 500 μL PBS buffer solution. The carboxyl groups of HS-PEG-COOH modified on Au NPs were activated by adding 5 μL of 50 mM EDC and 5 μL of 10 mM NHS solution and reacted at room temperature for 1 h. Then the mixture was centrifuged at 6000 rpm for 6 min to remove the excess EDC and NHS and resuspended in 500 μL PBS buffer solution. Afterward, 10 μL of 1 mg mL^{-1} goat anti-human IgG was added. After gently shaking for 2 h, the mixture was centrifuged at 6000 rpm for 6 min to remove the excess antibodies and resuspended in 500 μL PBS buffer solution containing 0.033% BSA and stored at 4 °C for future use.

The process of gold film modification was similar to Au NPs. As shown in Fig. 2, the gold films were first immersed in 1 mL of 10^{-3} M MUA solution under continuous shaking at room temperature. After 12 h, the gold films were rinsed three times with deionized water. The carboxyl groups of MUA were activated by immersing the gold films in a mixture solution which contained 500 μL of 50 mM EDC and 500 μL of 10 mM NHS solution. After 1 h, the gold films were rinsed with PBS buffer solution and deionized water three times each. Then 30 μL of 1 mg mL^{-1} goat anti-human antibody solution was pipetted onto the gold film, and the gold films were subsequently incubated in a humidity chamber at room temperature. After 2 h, the gold films were rinsed with PBS buffer solution and deionized water three times each to remove the unbound antibodies. Subsequently, 30 μL of 0.033% BSA was pipetted onto the gold film at room temperature for 1 h to block these unreacted sites. Then the gold films were rinsed with PBS buffer solution and deionized water three times each to remove excess BSA.

The last step is to form the NPOM biosensor. The prepared gold film was first immersed in 900 μL of human IgG solutions at different concentrations under continuous shaking at room temperature. After 2 h, the gold films were rinsed with deionized water and PBS buffer solution three times each. Then 30 μL of the prepared antibody-conjugated Au NP solution was pipetted onto the antigen-conjugated gold film and incubated in a humidity chamber at room temperature. Two hours later, the gold films were rinsed with PBS buffer solution and deionized water five times each, and then allowed to dry for detection.

In the dark-field scattering spectral measurement of 40, 60, 80, and 100 nm Au NPs, a 1 nm Al_2O_3 layer was grown on the surface of the gold film through atomic layer deposition at 120 °C. Then different sizes of Au NPs were drop-coated onto the substrate.

For SERS-based immunoassay, SERS nanotags were prepared. The process of preparation of SERS nanotags is similar to the preparation of antibody conjugated Au NPs mentioned above. First, 3 μL of 10^{-3} M 4-MBA solution was added to 500 μL of Au NP solution and shaken for 10 min before adding HS-PEG-COOH solution. Then the following steps remain unchanged. The modification of the gold film is the same as above. Lastly, 30 μL of the prepared SERS nanotag solution was pipetted onto the antigen-conjugated gold film. After 2 h, the gold films were rinsed with PBS buffer solution and deionized water five times each, and then allowed to dry for detection.

Optical measurements

Dark-field images were obtained using a 100× dark-field objective lens (Olympus, NA = 0.9), a commercial illuminator (Olympus BX51) with a dark-field specified module, and a CCD camera (Tucsen, TCH-1.4CICE) under the irradiation of a halogen lamp. Briefly, unpolarized white light from the halogen lamp was directed by the illuminator and focused on the sample by the 100× dark-field objective lens. Then the scattering light from the Au NPs was collected by the same objective lens and directed onto the CCD camera for imaging or to a spectrometer (Renishaw, inVia) to record the dark-field scattering spectra. The integration time was 10 seconds.

Raman spectra were recorded on a spectrometer, using a 633 nm laser with a power of 2.8 mW as the excitation source, in conjunction with a grating of 1800 lines per mm. A 20× objective lens (Olympus, NA = 0.45) was used to collect the Raman signal, and the diameter of the laser spot was 10 μm. The integration time was 10 seconds.

Simulations

Dark-field scattering spectral simulations were performed using a commercial finite element method package, COMSOL Multiphysics 5.2. The dispersive dielectric function of gold was taken from the experimental data by Johnson and Christy[42] and the refractive index of protein and SiO_2 is 1.5. The diameter of the Au NP in the simulation is 60 nm, taken from the scanning electron microscopy images. The gap between the Au NP and gold film is 1.3 nm. To simulate the scattering of the NPOM and NP on the SiO_2 systems, a linear polarized plane wave with an incident angle of 64°, which corresponds to the NA of the objective (NA = 0.9), was first utilized to excite the system in the absence of the Au NP. A periodic boundary condition was used to mimic an infinite large background field. Then, the scattering of the NPOM and NP on the SiO_2 systems was excited by the background field. Time-averaged power flow

was collected to simulate the far-field Rayleigh scattering spectra.

Conflicts of interest

There are no conflicts to declare.

Acknowledgements

This work was supported by the National Natural Science Foundation of China (Grant No. 91850207, 11674255, and 11674256) and the National Key R&D Program of China (Grant No. 2017YFA0303504 and 2017YFA0205800).

References

1 A. Alshannaq and J.-H. Yu, *Int. J. Public Health*, 2017, **14**, 632.
2 R. M. Lequin, *Clin. Chem.*, 2005, **51**, 2415–2418.
3 Y. Ueno, S. Nagata, T. Tsutsumi, A. Hasegawa, M. F. Watanabe, H. D. Park, G. C. Chen, G. Chen and S. Z. Yu, *Carcinogenesis*, 1996, **17**, 1317–1321.
4 D. M. Rissin, C. W. Kan, T. G. Campbell, S. C. Howes, D. R. Fournier, L. Song, T. Piech, P. P. Patel, L. Chang, A. J. Rivnak, E. P. Ferrell, J. D. Randall, G. K. Provuncher, D. R. Walt and D. C. Duffy, *Nat. Biotechnol.*, 2010, **28**, 595–599.
5 Z. Wang, S. Zong, L. Wu, D. Zhu and Y. Cui, *Chem. Rev.*, 2017, **117**, 7910–7963.
6 S. Laing, K. Gracie and K. Faulds, *Chem. Soc. Rev.*, 2016, **45**, 1901–1918.
7 J. Hwang, S. Lee and J. Choo, *Nanoscale*, 2016, **8**, 11418–11425.
8 S. M. Tabakman, L. Lau, J. T. Robinson, J. Price, S. P. Sherlock, H. Wang, B. Zhang, Z. Chen, S. Tangsombatvisit, J. A. Jarrell, P. J. Utz and H. Dai, *Nat. Commun.*, 2011, **2**, 466.
9 B. Zhang, R. B. Kumar, H. Dai and B. J. Feldman, *Nat. Med.*, 2014, **20**, 948–953.
10 D. F. Cruz, C. M. Fontes, D. Semeniak, J. Huang, A. Hucknall, A. Chilkoti and M. H. Mikkelsen, *Nano Lett.*, 2020, **20**, 4330–4336.
11 J.-F. Masson, *ACS Sens.*, 2017, **2**, 16–30.
12 K. M. Mayer, S. Lee, H. Liao, B. C. Rostro, A. Fuentes, P. T. Scully, C. L. Nehl and J. H. Hafner, *ACS Nano*, 2008, **2**, 687–692.
13 J. Homola, *Chem. Rev.*, 2008, **108**, 462–493.
14 S. Chen, M. Svedendahl, R. P. Van Duyne and M. Kall, *Nano Lett.*, 2011, **11**, 1826–1830.
15 D. Du, L. Wang, Y. Shao, J. Wang, M. H. Engelhard and Y. Lin, *Anal. Chem.*, 2011, **83**, 746–752.
16 S. Mubeen, S. Zhang, N. Kim, S. Lee, S. Kraemer, H. Xu and M. Moskovits, *Nano Lett.*, 2012, **12**, 2088–2094.
17 J. J. Mock, M. Barbic, D. R. Smith, D. A. Schultz and S. Schultz, *J. Chem. Phys.*, 2002, **116**, 6755–6759.
18 M. Hu, A. Ghoshal, M. Marquez and P. G. Kik, *J. Phys. Chem. C*, 2010, **114**, 7509–7514.
19 J. Ma, L. Zhan, R. S. Li, P. F. Gao and C. Z. Huang, *Anal. Chem.*, 2017, **89**, 8484–8489.
20 F. Qi, Y. Han, Z. Ye, H. Liu, L. Wei and L. Xiao, *Anal. Chem.*, 2018, **90**, 11146–11153.
21 Z. Ye, R. Weng, Y. Ma, F. Wang, H. Liu, L. Wei and L. Xiao, *Anal. Chem.*, 2018, **90**, 13044–13050.
22 T. Li, X. Xu, G. Zhang, R. Lin, Y. Chen, C. Li, F. Liu and N. Li, *Anal. Chem.*, 2016, **88**, 4188–4191.
23 J. J. Mock, D. R. Smith and S. Schultz, *Nano Lett.*, 2003, **3**, 485–491.
24 A. D. McFarland and R. P. Van Duyne, *Nano Lett.*, 2003, **3**, 1057–1062.
25 W. Chen, H. Hu, W. Jiang, Y. Xu, S. Zhang and H. Xu, *Chin. Phys. B*, 2018, **27**, 107403.
26 W. Chen, S. Zhang, M. Kang, W. Liu, Z. Ou, Y. Li, Y. Zhang, Z. Guan and H. Xu, *Light: Sci. Appl.*, 2018, **7**, 56.
27 C. Ciraci, R. T. Hill, J. J. Mock, Y. Urzhumov, A. I. Fernandez-Dominguez, S. A. Maier, J. B. Pendry, A. Chilkoti and D. R. Smith, *Science*, 2012, **337**, 1072–1074.
28 G.-C. Li, Q. Zhang, S. A. Maier and D. Lei, *Nanophotonics*, 2018, **7**, 1865–1889.
29 J. J. Baumberg, J. Aizpurua, M. H. Mikkelsen and D. R. Smith, *Nat. Mater.*, 2019, **18**, 668–678.
30 L. Shao, X. Wang, H. Xu, J. Wang, J.-B. Xu, L.-M. Peng and H.-Q. Lin, *Adv. Opt. Mater.*, 2014, **2**, 162–170.
31 C.-Y. Poon, L. Wei, Y. Xu, B. Chen, L. Xiao and H.-W. Li, *Anal. Chem.*, 2016, **88**, 8849–8856.
32 S.-Y. Chen, J. J. Mock, R. T. Hill, A. Chilkoti, D. R. Smith and A. A. Lazarides, *ACS Nano*, 2010, **4**, 6535–6546.
33 P. Nordlander and E. Prodan, *Nano Lett.*, 2004, **4**, 2209–2213.
34 J. Gao, X. Huang, H. Liu, F. Zan and J. Ren, *Langmuir*, 2012, **28**, 4464–4471.
35 X. Qian, X.-H. Peng, D. O. Ansari, Q. Yin-Goen, G. Z. Chen, D. M. Shin, L. Yang, A. N. Young, M. D. Wang and S. Nie, *Nat. Biotechnol.*, 2008, **26**, 83–90.
36 J. Ni, R. J. Lipert, G. B. Dawson and M. D. Porter, *Anal. Chem.*, 1999, **71**, 4903–4908.
37 S. M. Nie and S. R. Emery, *Science*, 1997, **275**, 1102–1106.
38 K. Kneipp, Y. Wang, H. Kneipp, L. T. Perelman, I. Itzkan, R. Dasari and M. S. Feld, *Phys. Rev. Lett.*, 1997, **78**, 1667–1670.
39 H. X. Xu, E. J. Bjerneld, M. Kall and L. Borjesson, *Phys. Rev. Lett.*, 1999, **83**, 4357–4360.
40 M. Yi, D. Zhang, P. Wang, X. Jiao, S. Blair, X. Wen, Q. Fu, Y. Lu and H. Ming, *Plasmonics*, 2011, **6**, 515–519.
41 J. Baniukevic, I. H. Boyaci, A. G. Bozkurt, U. Tamer, A. Ramanavicius and A. Ramanaviciene, *Biosens. Bioelectron.*, 2013, **43**, 281–288.
42 P. B. Johnson and R. W. Christy, *Phys. Rev. B: Solid State*, 1972, **6**, 4370–4379.